Characterization of volume strain at large deformation under uniaxial tension in high-density polyethylene

Frederic Addiego, Abdesselam Dahoun, Christian G'Sell *, Jean-Marie Hiver

Laboratoire de Physique des Matériaux (UMR CNRS 7556), Ecole des Mines, INPL, Parc de Saurupt, 54042 Nancy, France

Abstract

The intensity and origin of volume changes under uniaxial tension is investigated at room temperature in high-density polyethylene samples with a large initial degree of crystallinity. At the macroscopic scale, volume strain is defined as the trace of the finite strain tensor whose components are recorded in situ by means of a 2D video extensometer within a representative volume element situated at the center of the neck. At the microscopic scale, volume strain is ascribed to the competition of cohesive mechanisms and non-cohesive mechanisms. The former are associated both to the packing of oriented chains in the amorphous phase (compaction) and to the decrease of crystallinity (dilatation), as characterized by wide-angle X-ray diffraction analysis. The latter are due to the development of crazes and voids (dilatation) while the spherulitic morphology is progressively transformed into a highly fibrillated structure, as revealed by scanning electron microscopy. Detailed evaluation of the relative importance of these two classes of mechanisms shows that they compensate nearly exactly at moderate strains, so that volume strain is very small in the first stage of the tensile tests. By contrast, the effect of cavitation becomes prominent at large deformation, so that the overall dilatation reaches more than 30% before rupture. It is demonstrated that volume strain measurements obtained from mechanical testing and from microstructural investigation agree fairly satisfactorily.
© 2006 Elsevier Ltd. All rights reserved.

Keywords: Polyethylene; Plastic deformation; Cavitation

1. Introduction

Mechanical properties that govern the application of structural polymers are intimately controlled by multiscale deformation mechanisms ranging from nanometric configuration changes to mesoscopic strain fields. More specifically, the high toughness of most semi-crystalline polymers makes them suitable for the fabrication of products subjected to severe conditions (impact loading, low temperature applications, creep, fatigue, etc.). In particular, high-density polyethylene (HDPE for short) has received much attention in the past and is often considered as a 'model' polymer for the study of the mechanical behavior of crystallized polymers. Among the microstructural aspects of HDPE deformation, the transformation upon stretching of the lamellar morphology into a highly fibrillated structure has been characterized in many works [1–7]. However, most of these studies were essentially qualitative and the detailed modeling of microstructure-properties relationships is far from being completed to date. This is notably because early plastic instability (necking under uniaxial tension) makes difficult the characterization of intrinsic stress–strain behavior at prescribed temperature and strain rate.

Only a few workers [8–12] have overcome this problem by measuring in real time the cross-section area at the center of the neck by means of mechanical or optical transducers. As such, under the assumption of constant density, they were capable of deriving the response of the material within a very small representative volume element (RVE) in which stresses and strains are supposed to be nearly homogeneous. Also, they controlled the actuator of the testing machine in such a way that strain rate was kept constant in the RVE. The constitutive equations determined by this local approach are directly applicable by mechanical engineers for the design of complex parts by means of finite-element codes, in view of optimizing their geometry for given loading conditions.

Furthermore, the phenomenological response of semi-crystalline polymers was ascribed to macromolecular processes like viscoelastic relaxation of monomer conformations, unraveling of amorphous chains, crystal glide and rotation,

---

* Corresponding author. Tel.: +33 3 83 58 41 54; fax: +33 3 83 58 43 44.
E-mail address: gsell@mines.inpl-nancy.fr (C. G'Sell).

texture formation, etc. [2,6,13,14]. Again, for this multiscale modeling, HDPE has been often taken as the reference semi-crystalline polymer.

Plastic deformation of most semi-crystalline polymers under uniaxial tension induces an important whitening that is visible at the naked eye. Density measurements on stretched samples revealed significant dilatation [6] that has been ascribed to non-cohesive damage mechanisms (void formation, crazing, crack growth). However, in the mechanical design of polymer structures subjected to plastic deformation, the simulations are recurrently based on isochoric assumption, like if cavitation effects were negligible. This situation is mainly due to the difficulty of measuring volume changes with enough precision after neck formation within the same RVE where axial stress and strain are determined.

Mechanical extensometers were tentatively developed to analyze multiaxial deformation in samples under tension [15–18]. These techniques marked the first steps towards the correct assessment of volume variation, but the calibrated region investigated was often too large with respect to the characteristic length of the necks. Furthermore, they were delicate to manipulate, susceptible to notch the material, and usually limited to ambient temperature. Hybrid techniques, using a laser sensor coupled with a mechanical extensometer [19], have improved somewhat the precision of the volume variation measurements, but were essentially limited to homogeneously deforming materials. Significant progress and better flexibility was recently obtained by using video-extensometers [20,21], but they failed for specimens with marked necks. A special video system applicable to materials after the onset of necking was also developed [22] but its precision is somewhat limited. Whatever the performances of their systems, these pioneer authors have clearly established the fact that significant dilatation occurs in plastically stretched polymers. As such, they have initiated a fruitful discussion about the microstructural processes responsible for this unexpected phenomenon.

Continuous inventive activity in this laboratory was recently focused on a new video-controlled apparatus (VidéoTraction[©] by G'Sell et al. [23]) capable of recording in real time the evolution of volume changes vs. axial strain in the RVE of tensile samples, in addition to the axial stress–strain curve, even after the onset of necking. In the case of glassy polymers (PET for example), important dilatation was recorded, which was correlated with the development of crazes [24]. In this paper, after recalling briefly the principal features of the novel system, we will examine the case of semi-crystalline HDPE. For this polymer, we will assess volume change effects during uniaxial tension at ambient temperature. Also, we will characterize the microstructural mechanisms inducing density modification in the amorphous phase and among the crystals. Subsequently, we will critically review all these facts in the perspective of a global model taking into account all aspects of polymer deformation, including elasticity, amorphous chain orientation, crystalline plasticity and cavitation.

2. Experimental methods

2.1. Material

The high-density polyethylene (HDPE) investigated in this work was manufactured by Du Pont Canada Co. under the reference Sclair 2907. Its number and weight average macromolecular weights, determined by previous authors (e.g. [25]) are equal to $\bar{M}_n = 16,800$ and $\bar{M}_w = 93,600$ g/mol, respectively. Solid cylinders, 110 mm in diameter, were specially extruded by the Plastifab Company of Montréal, Canada. In this process, the material is slowly cooled in air after getting out of the die in order to minimize internal stresses and favor homogeneous microstructure. Plates, 7 mm thick, are cut out of the core region of the cylinders following planes parallel to the extrusion axis. The density of the material, measured by hydrostatic weighting, is $\rho = 0.962$ g/cm^3. Based on values published in the literature [26] for perfectly crystalline and amorphous phases ($\rho_c = 0.997$ and $\rho_a = 0.854$ g/cm^3, respectively), the weight index of crystallinity is found to be equal to 78%. This value is confirmed by differential scanning calorimetry (DSC) that shows a melting point at 136 °C, with a heat of fusion equal to 0.292 kJ/g, corresponding to an index of crystallinity equal to 77 wt%. The crystalline morphology is characterized by large spherulites (average diameter of about 50 μm) with regularly twisted lamellae. The long period of the semi-crystalline stacks, as determined by small-angle X-ray scattering (SAXS), is equal to 27.3 nm that gives, in conjunction with the crystallinity ratio, an average lamellar thickness of 20.7 nm. The high crystal-linity and coarse microstructure of Sclair 2907 HDPE, already investigated by previous authors [27], are due to its very low content in catalytic residues and the absence of nucleating agents.

2.2. Video-controlled tensile tests

The video-controlled mechanical testing method utilized here is the latest version of the VidéoTraction[©] system invented by two of the authors (G'Sell and Hiver [9,23,24]). It is developed by Apollor SA (Vandoeuvre, France). It gives access to the plastic response of polymers under uniaxial tension from video measurements performed locally at the center of the neck. As we will recall it briefly, the novel version gives access not only to the axial stress–strain curve, but also to the local evolution of volume strain during the test.

The test samples are machined from the polished plates using a computer-controlled milling machine (CharlyRobot CRA4) following the shape represented in Fig. 1. The calibrated zone is a parallelepiped of $34 \times 7.6 \times 6$ mm^3, the median region of it having a reduced width of 6.8 mm and a local radius of curvature of 15 mm in order to localize necking in this predetermined zone. Seven dot markers, made of flexible fluorescent ink, are printed on the front flat face of the sample. Five of these dots are aligned and equally spaced in the tensile direction, x_3, while the two others are aligned with the central dot along the transverse direction, x_1.
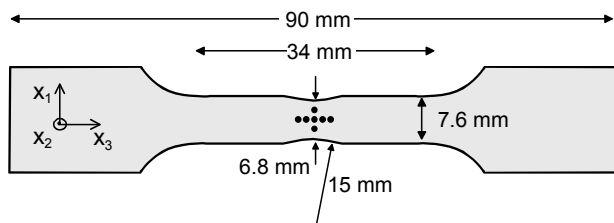
Fig. 1. Tensile sample with seven markers.

The mechanical tests are carried out with a servo-hydraulic machine (MTS 810). The seven fluorescent markers, illuminated with an ultraviolet lamp, are followed in real time during the tensile tests by means of a CCD camera (resolution 800×600 pixels) interfaced with a microcomputer through a video interface board (Genesis, by Matrox, Canada). Also the load cell and the actuator of the tensile machine are interfaced with the microcomputer to record the applied load, P, and to regulate the speed of the actuator, respectively, (Fig. 2). The procedure performed from each digitized image was detailed in a previous paper [24]. We just summarize below its main steps.

The system determines the (x_1, x_3) coordinates of the center of gravity of each dot. Subsequently, the software assesses dynamically the distances between dots aligned in both axial and transverse directions and calculates the 'true' strains following Hencky's definition: (i) the axial strain at successive couples of markers, for example $\varepsilon_{33}(AB) = \ln(AB/A_0B_0)$, (ii) the transverse strain at the couple of markers F and G, $\varepsilon_{11}(FG) = \ln(FG/F_0G_0)$. The RVE considered in this work is the thinnest material slice that includes the centers of gravity of the three markers F, C and G. Its axial dimension increases during the tensile test, while its transversal dimensions decrease. The axial true strain in the RVE, ε_{33}, is obtained by a polynomial interpolation from the four axial strains $\varepsilon_{33}(AB)$, $\varepsilon_{33}(BC)$, $\varepsilon_{33}(CD)$ and $\varepsilon_{33}(DE)$ (Fig. 3) and the transverse strains in the RVE, ε_{11} and ε_{22}, are equal to ε_{11} (FG) if the strain field is transversally isotropic in the center of the neck. This assumption was previously made by several authors [17,19,28,29] and it is validated in our samples by checking that the width and thickness of the neck are proportionally reduced during deformation. Lastly, the volume strain in the
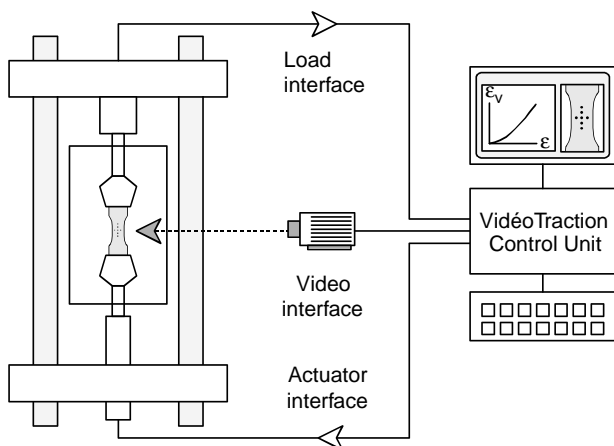

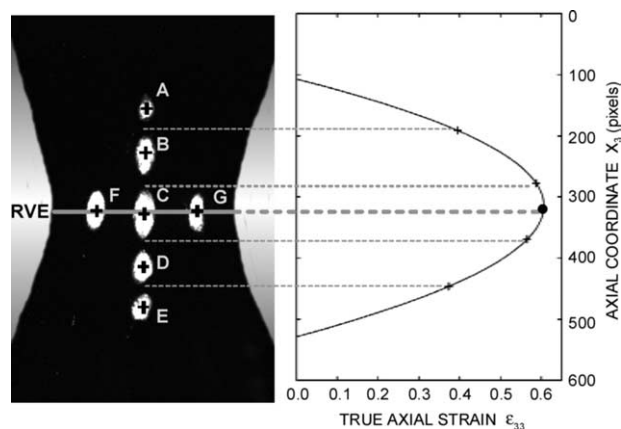Fig. 2. General diagram of the VidéoTraction© system.

Fig. 3. Determination of true axial strain in the representative volume element (RVE).

RVE, ε_v, is simply computed from the trace of the true strain tensor, $\varepsilon_v = \varepsilon_{11} + \varepsilon_{22} + \varepsilon_{33}$. The accuracy of strain measurements is about 10^{-3}. The axial true stress (Cauchy stress) is determined in the same RVE as the load per unit actual cross-section: $\sigma_{33} = (P/S_0)\exp(-2\varepsilon_{11})$ where S_0 is the initial cross-section. All measurements are performed at a maximum rate of 50 images per second. An important feature of our protocol is that the speed of the servo-hydraulic actuator is regulated in real time in such a way that the instantaneous true strain in the RVE, $d\varepsilon_{33}/dt$, remains constant during the course of the tests [24].

The tensile tests are performed at 23 °C under different strain rates from 10^{-4} to 5×10^{-3} s^{-1}. In order to characterize the evolution of the microstructure during the plastic deformation, different tests are carried out at 10^{-3} s^{-1} until various strains are attained under load: $\varepsilon_{33} = 0.2$, 0.4, 0.6, 0.8, 1.0, 1.2 and 1.5. For each test, the sample is unloaded and the evolution of the axial true strain and volume strain are followed during 3 h. At the end of this period, the residual true strain and volume strain, ε_{33r} and ε_{vr}, are recorded.

2.3. Microscopic investigation

Samples to be characterized by scanning electron microscopy (SEM) are treated according to the following protocol: (i) heads are cut, (ii) RVE is marked by a small notch in such a way that it could be precisely located in the SEM, (iii) surface is abraded down to mid-thickness and finely polished, (iv) spherulitic structure is revealed by etching for 18 h in a reagent made up of 65.8 wt% H_2SO_4, 32.9 wt% H_3PO_4 and 1.3 wt% $KMnO_4$ [30,31], (v) specimen is rinsed thoroughly, (vi) exposed surface is coated with a thin gold layer. The SEM utilized is a field-effect gun model (Philips FEG XL 30). The secondary electron (SE) mode allowed a detailed examination of the semi-crystalline structure, through the differential relief between lamellae and amorphous interlayers, while the back scattered electron mode (BSE) revealed better the presence of cavities that appear darker than the rest of the material. The intensity of the digitized micrographs is defined on a 256 gray

scale and processed with the Aphelion© software (Adcis and AAI Inc.).

2.4. X-ray diffraction

Non-deformed and deformed samples are analyzed by wide-angle X-ray scattering (WAXS). The selected tension and the intensity are 30 kV and 40 mA, respectively. The wavelength used is $K_{\alpha 1}$ copper radiation ($\lambda = 0.154$ nm), selected by means of a parabolic multilayer mirror (Osmic) and a cylindrical capillary. In this diffraction system (Inel, France), the sample tensile axis is perpendicular to the incident X-ray beam. The 2D transmission pattern, intercepted by a Fujifilm image plate normal to the beam, is revealed with the adapted scanner (Fujifilm BAS 5000) with a maximum resolution of 25 μm, the image being readily obtained in digital form with a PC microcomputer. Before analyzing the WAXS pattern, an absorption correction is brought to the intensity distribution by the Lambert equation, $I = I_0 \exp(\mu t / \cos(2\theta))$, where 2θ is the diffraction angle, μ the absorption coefficient equal in this case to 3.85 cm^{-1} [32] and $t = 0.08$ cm the thickness of the sample. Subsequently, the corrected diffraction curve, $I(2\theta)$, is analyzed using the PeakFit© software (SPSS Inc.) in view of extracting the different components: (i) background, (ii) crystalline peaks and, (iii) amorphous bump (amorphous 'halo'). Following previous authors [14,33], we fit the contributions of amorphous and crystalline phases by a series of Gaussian curves of different heights and widths. We will examine later in this paper, how this information gives access to the degree of orientation, the crystallinity index and the average distance between diffracting molecules.

3. Experimental results

3.1. Mechanical behavior

3.1.1. Behavior of the material during continuous loading at constant strain rate

Fig. 4(a) shows the evolution of true axial stress, σ_{33}, vs. true axial strain, ε_{33}, for the HDPE under uniaxial tension at 23 °C for a strain rate $\dot{\varepsilon}_{33} = 10^{-3}$ s^{-1}. Three successive stages are noted. The first one ($\varepsilon_{33} = 0$–0.14) is called 'viscoelastic stage' for simplicity, although it was shown by previous authors [6,34,35] that it is due to successive and/or concurrent mechanisms including: (i) elastic deformation of van der Waals bonds, (ii) recoverable chain conformation changes in amorphous phase and, (iii) early plasticity due to glide processes in crystalline lamellae. The initial slope of the stress–strain curve corresponds to the elastic Young's modulus ($E \approx 1500$ MPa). The yield point is defined when stress passes through a rounded-off maximum at $\sigma_{33}^y = 29.8$ MPa. It also corresponds to the onset of unstable necking. The second stage ($0.14 < \varepsilon_{33} < 0.5$) is marked by a small but significant stress decrease. The last stage ($\varepsilon_{33} = 0.5$–1.5) corresponds to the plastic hardening of the material, σ_{33} increasing from 29.2 to 42.3 MPa.
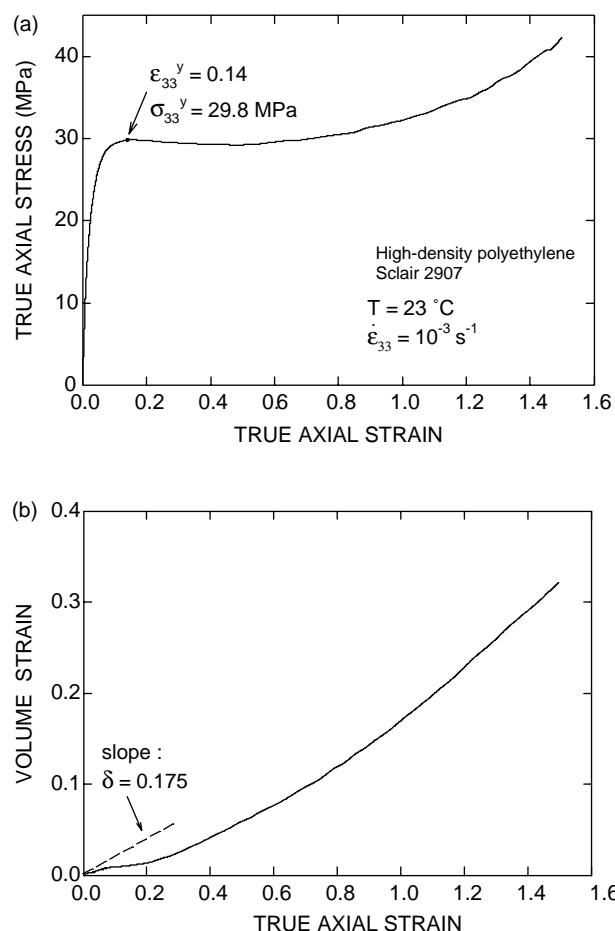

Fig. 4. Tensile behavior of the HDPE at 23 °C for a strain rate of 10^{-3} s^{-1}. (a) Axial stress vs. axial strain; (b) volume strain vs. axial strain.

The evolution of volume strain, $\varepsilon_v = \varepsilon_{11} + \varepsilon_{22} + \varepsilon_{33}$, vs. true axial strain, ε_{33}, is shown in Fig. 4(b). This information constitutes the novel feature of the VidéoTraction© system. The initial slope of the curve, equal to 0.175, is readily correlated with the elastic Poisson's ratio, $\nu = -\varepsilon_{11}/\varepsilon_{33}$, by the relation: $d\varepsilon_v/d\varepsilon_{33} = (1 - 2\nu)$. Consequently, one gets $\nu = 0.41$. For the rest of the viscoelastic stage, it is noted that the slope decreases. A tangent Poisson's ratio can be defined as $\nu_t = -d\varepsilon_{11}/d\varepsilon_{33}$. In this case, it reaches a maximum value $\nu_t = 0.48$ at the yield point. Once plastic stage begins, the dilatation rate increases again. Consequently, the tangent Poisson's ratio decreases until it reaches $\nu_t = 0.33$ at the end of the test, while the volume strain attains $\varepsilon_v = 0.32$ at $\varepsilon_{33} = 1.5$.

3.1.2. Influence of strain rate

The curves in Fig. 5 show the influence of strain rate on stress and volume strain. As stated earlier for another HDPE grade [8], one notes that flow stress globally increases with strain rate (Fig. 5(a)). This influence is usually quantified by the 'strain rate sensitivity coefficient' defined as $\gamma = [\partial \ln \sigma_{33} / \partial \ln \dot{\varepsilon}_{33}]_{\varepsilon_{33}}$. Here, on average, this coefficient is of the order of 0.08. It is interesting to remark that this value is higher than for glassy polymers. Also it is found (Fig. 5(b)) that volume strain depends on strain rate. At the slowest rate
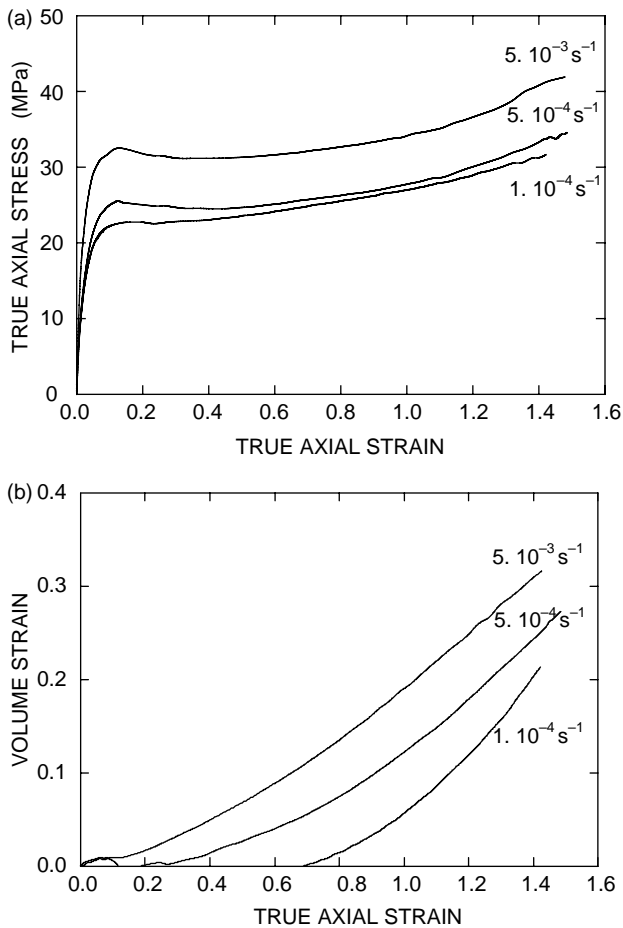
Fig. 5. Influence of strain rate on the tensile behavior of the HDPE at 23 °C. (a) Axial stress vs. axial strain; (b) volume strain vs. axial strain.

Fig. 6. Evolution of axial stress and volume strain vs. axial strain of HDPE during monotonous loading at 10^{-3} s^{-1} (0→1), unloading (1→2) and recovery at zero stress for 3 h (2→3).

($\dot{\varepsilon}_{33} = 1 \times 10^{-4}$ s^{-1}), volume stays nearly constant for a while (even a small compaction is recorded under tension) and ultimate dilatation begins when axial strain gets larger than $\varepsilon_{33} \approx 0.8$. By contrast, for the fastest rates, the onset of volume dilatation is much earlier.

3.1.3. Behavior of the material during unloading and recovery

The evolution of true axial strain and volume strain during unloading and recovery sequences are represented in Figs. 6–8. In Fig. 6, the specimen is deformed until strain under load reaches 1.0, subsequently unloaded (at a strain rate opposite to the initial loading rate) and finally left to recover at zero stress for 3 h. The $\sigma_{33}(\varepsilon_{33})$ curve shows a strain decrease from 1.0 to 0.93 (-7%) during unloading, and from 0.93 to 0.71 (-24%) during the recovery period. For its part the $\varepsilon_{v}(\varepsilon_{33})$ curve shows that dilatation decreases from 0.17 to 0.14 during unloading (-24%), and furthermore from 0.14 to 0.04 during recovery (-70%). As such, the decrease of volume strain during unloading and recovery is much more important than the decrease of axial strain. It is seen in Fig. 7 that the decay of axial and volume strains is nearly stabilized after a 3 h recovery period. Consequently, it can be legitimately supposed that the samples practically stable during one or two days after the end
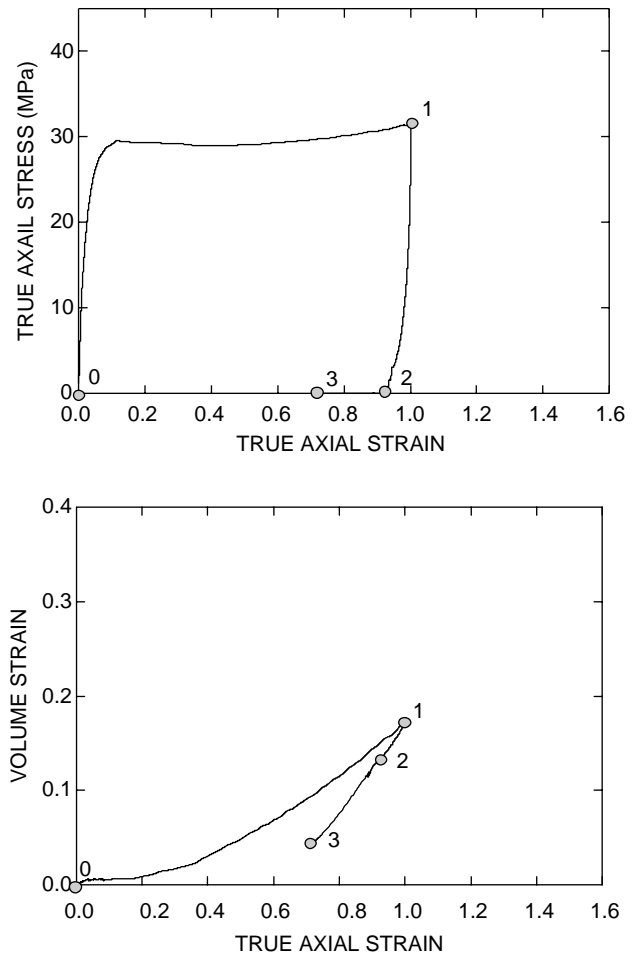
of the test, this delay being enough to perform the microstructural characterization.

Lastly, Fig. 8 shows volume strain vs. axial strain curves obtained for loading/unloading experiments (at $\dot{\varepsilon}_{33} = 10^{-3}$ s^{-1}) run up to different levels of strain. It is noted that the loaded–unloaded volume strain amplitude is maximum for moderate axial strains. The extreme case is for the specimen subjected to axial and volume strain is equal $\varepsilon_{33}=0.4$ and $\varepsilon_{v}=0.026$, respectively. The corresponding residual values after unloading are $\varepsilon_{33r}=0.14$ and $\varepsilon_{vr}=-0.02$. Globally, the relative variation of volume strain upon unloading decreases when applied strain increases: $(\varepsilon_{v}-\varepsilon_{vr})/\varepsilon_{v}$ passes from 128 to 41% when the maximum strain, ε_{33}, passes from $\varepsilon_{33}=0.2$ to $\varepsilon_{33}=1.5$. The important consequence is that a net residual compaction is recorded for loaded strains smaller than $\varepsilon_{33} \approx 0.8$, while residual volume strain remains positive for higher applied strains.

3.2. Post-mortem characterization

3.2.1. Microstructural investigation

The spherulitic morphology of the HDPE in its non-deformed state, observed by SEM, is shown in Fig. 9.
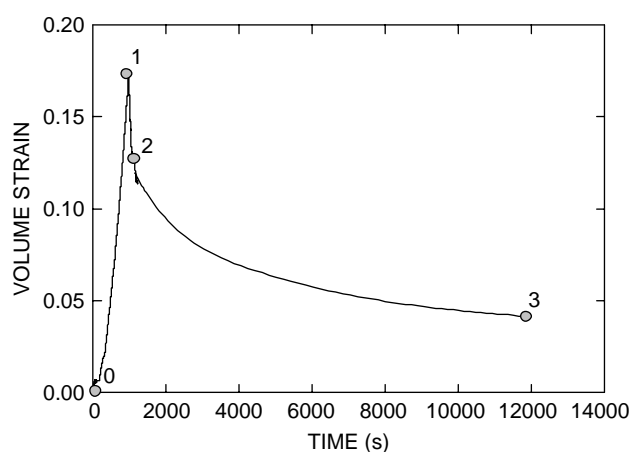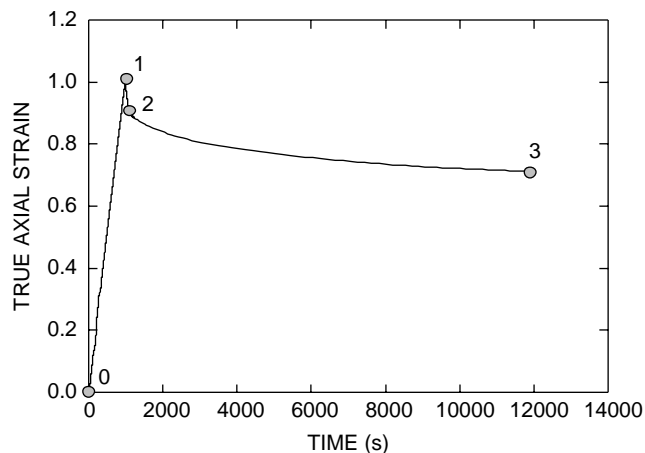
Fig. 7. Evolution of axial strain and volume strain vs. time of HDPE during monotonous loading at $10^{-3}\,\text{s}^{-1}$ ($0\rightarrow1$), unloading ($1\rightarrow2$) and recovery at zero stress for 3 h ($2\rightarrow3$).

Overlapping spherulites with an average diameter of about 50 μm are observed. They show banded morphology due to the presence of twisted lamellae, a feature commonly observed in HDPE and interpreted recently by a model based on
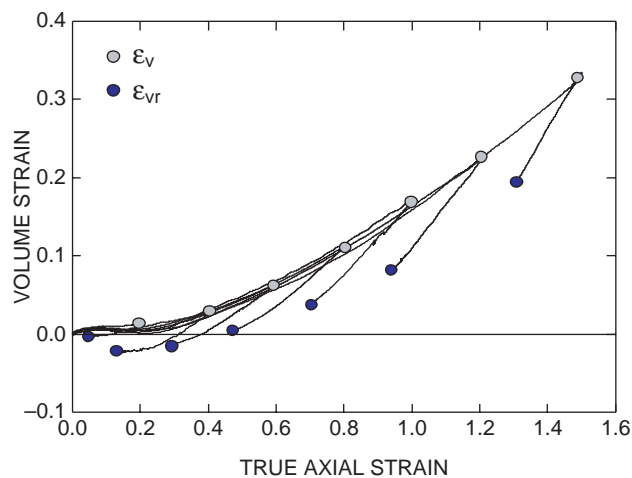

Fig. 8. Loading/unloading experiments up to different levels of axial strain (volume strain under load and residual volume strain after unloading are indicated).
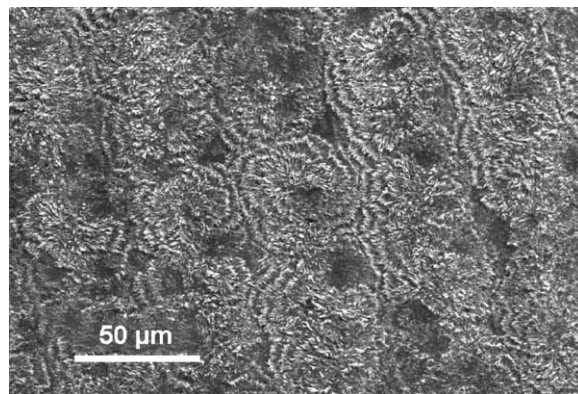

Fig. 9. Spherulitic morphology of homogeneous HDPE.

the reduction of surface stress of crystalline lamellae by re-ordering the fold surface through dislocation nucleation [36–39].

The evolution of microstructure at the center of the RVE is displayed in Fig. 10 for increasing levels of residual strain. For $\varepsilon_{33r}=0.05$ (Fig. 10(a)), a few crazes are observed in the equatorial zone of the spherulites, that is between lamellae more or less perpendicular to the tensile axis. Furthermore, for $\varepsilon_{33r}=0.71$ (Fig. 10(b)), evidence of inter-spherulitic decohesion is presented in addition to intra-spherulitic crazing. Later, for $\varepsilon_{33r}=0.93$ (Fig. 10(c)), the spherulites become highly fragmented. Only the polar zone of spherulites remains visible with its original features, while the equatorial zone is transformed into a fibrillar structure oriented parallel to the tensile axis, with extensive cavitation evidently coming from craze growth and coalescence. Finally, for $\varepsilon_{33r}=1.3$ (Fig. 10(d)), the RVE is completely transformed into micro-fibrillar structure whose important feature is a high-density of voids elongated along the stretching direction [1].

As illustrated in Fig. 11 for a residual strain of $\varepsilon_{33r}=0.48$, the micrographs obtained with the BSE detection mode gives optimum resolution of cavitation within the material. In such an image, the gray scale is in the range from 0 to 255: black corresponds to 0 and white to 255. In our protocol, 15 SEM images are analyzed at $\times2000$ magnification with each deformed and recovered sample. It is noted that most crazes appear with a gray level lower than 50, while the polymer bulk is characterized by higher levels. Consequently, assessing the surface of crazes, S_{cr}, where intensity is lower to an appropriate threshold gives access to the overall surface fraction of crazes, S_{cr}/S_0, where S_0 is the total surface of the micrograph.

The three curves at the top of the graph in Fig. 12, obtained from a series of specimens stretched at 23 °C for a strain rate of $10^{-3}\,\text{s}^{-1}$, show the evolution of the craze fraction with residual axial strain. They correspond to three values of the intensity threshold: 0, 25 and 50. Their relatively small divergence indicates the homogeneity of brightness within the craze population. From this observation, it is deduced that the gray level 25 constitutes a correct threshold for minimizing the experimental error in the determination of craze fraction. The corresponding curve illustrates quantitatively the gradual increase of S_{cr}/S_0 with axial strain.
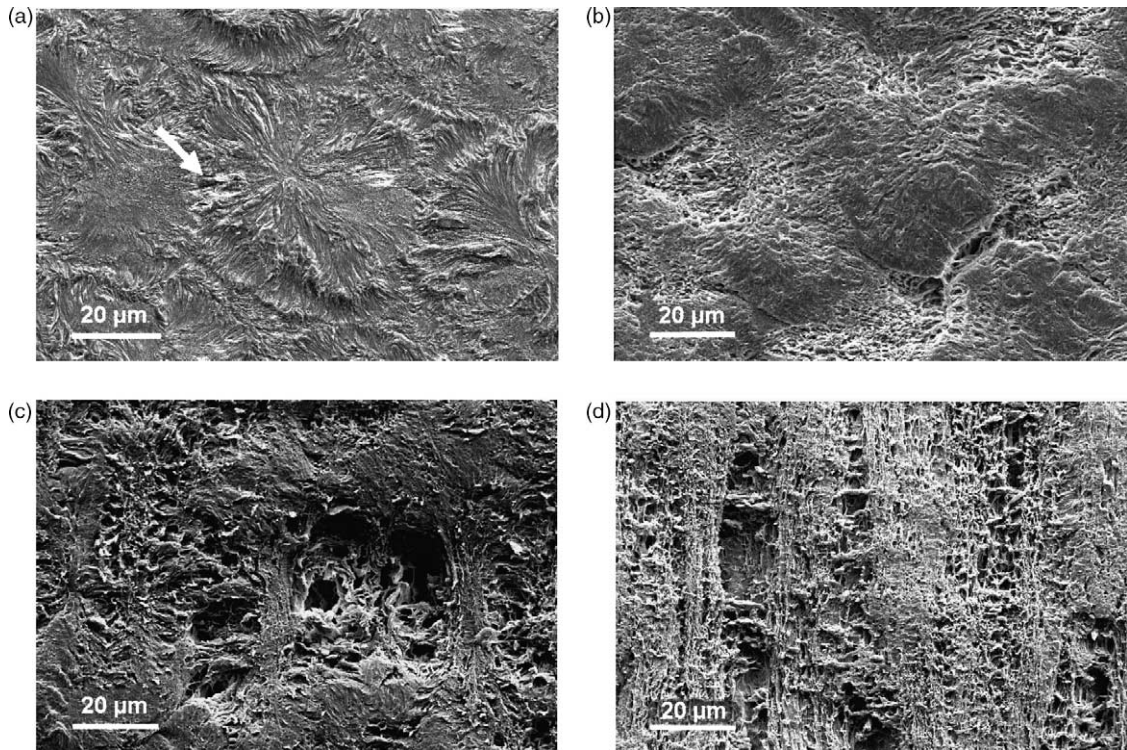
Fig. 10. SEM observation of cavitation mechanisms in HDPE during plastic deformation (tensile axis is vertical). (a) Equatorial crazes for $\varepsilon_{33r}=0.05$; (b) inter-spherulitic decohesion for $\varepsilon_{33r}=0.71$; (c) craze coalescence for $\varepsilon_{33r}=0.93$; (d) voids in fibrillar morphology for $\varepsilon_{33r}=1.30$.

However, the craze fraction assessed by the above protocol overestimates the actual void fraction in the deformed material since it includes unduly the solid space occupied by the micro-fibrils that were present before their elimination by the chemical attack. According to several authors [40–43], the volume fraction of micro-fibrils in the crazes represents about 40% for most polymers. Therefore, the actual void fraction within an exposed section should be estimated by $f_{vr}=0.6\times S_{cr}/S_0$. The curve at the bottom of Fig. 12 represents this corrected fraction. It is remarked that the maximum void fraction reaches the maximum value 0.21 for $\varepsilon_{33r}=1.3$.
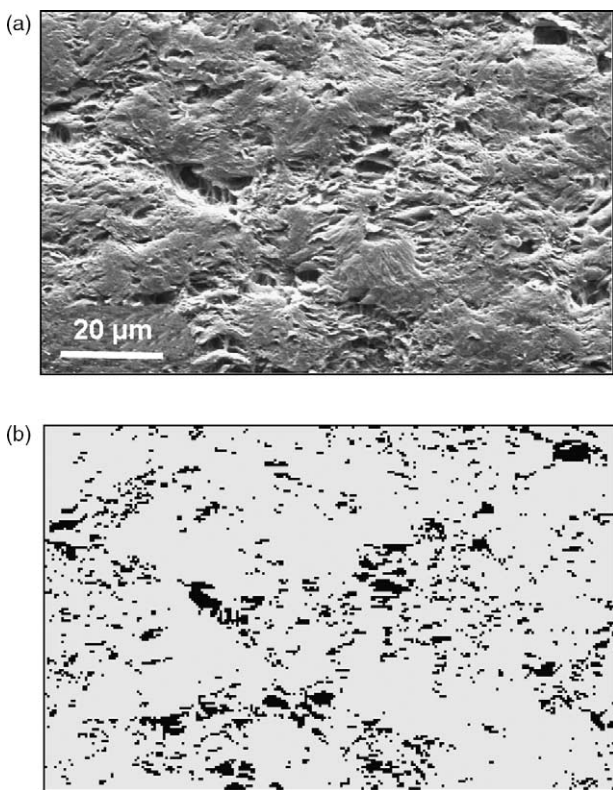

Fig. 11. SEM observation of HDPE microstructure with a residual strain of $\varepsilon_{33r}=0.48$ (tensile axis is vertical). (a) SE detection mode; (b) BSE detection mode.
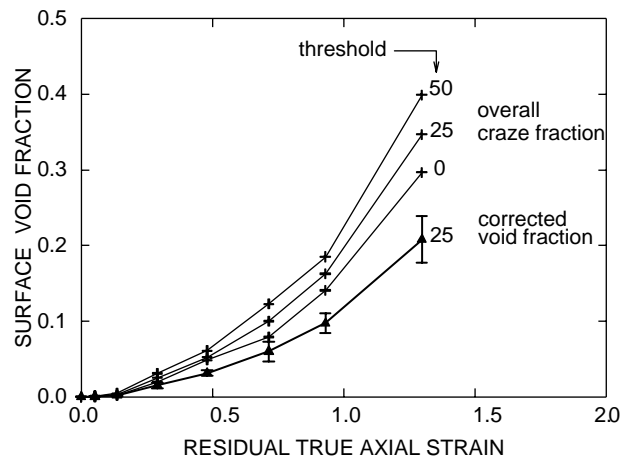

Fig. 12. Actual surface fraction of voids deduced from SEM micrographs vs. residual axial strain.
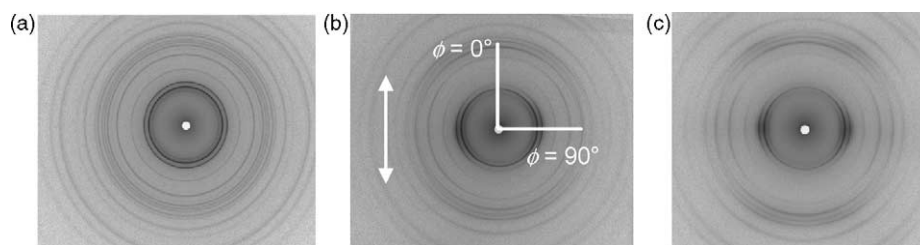
Fig. 13. WAXS patterns obtained with samples subjected to uniaxial stretching, unloading and recovery for residual strains equal to (a) 0.0; (b) 0.48; (c) 1.3.

3.2.2. X-ray characterization

The WAXS patterns $I(\phi,2\theta)$ corresponding to the residual strains of 0.0, 0.48, and 1.3 are displayed in Fig. 13. The non-deformed material is characterized by a set of concentric circles of different intensities, the intensity of each circle being homogeneous. When $\varepsilon_{33r}=0.48$, the intensity along the rings is inhomogeneous. In particular, for reflections with the planes parallel to chain axis, intensity is minimum at $\phi=0°$ and maximum at $\phi=90°$. This phenomenon increases with residual axial strain, as noticed on the X-ray diagram for $\varepsilon_{33r}=1.3$ (Fig. 13(c)). This observation is in line with a gradual rotation of chain axis toward tensile direction.

The scan, $I(2\theta)$, of the non-deformed polyethylene is shown in Fig. 14. The larger peaks, $(110)_o$ and $(200)_o$, come from the equilibrium orthorhombic phase (parameters: $a=0.738$, $b=0.492$ and $c=0.256$ nm). Secondarily the $(001)_m$ and $(200)_m$ peaks of the monoclinic phase are observed. This phase could have appeared under the effect of shear flow during the extrusion of the rods [44]. This transformation from orthorhombic to monoclinic also takes place under stress during the mechanical deformation of polyethylene and has been widely studied [7,45,46]. Finally, the $(100)_h$ peak reveals the presence of a minority pseudo-hexagonal phase investigated previously [47]. In addition to the crystalline peaks, the X-ray scan shows an amorphous 'bump' that is centered at $2\theta_a=20.63°$. Using areas of the peaks identified from $2\theta=15–45°$, the calculated crystallinity is $X_c=75$ wt% that corresponds fairly well to the value obtained by DSC.

Various scans $I(2\theta)$ corresponding to a residual strain of $\varepsilon_{33r}=0.48$ are represented in Fig. 15. We study the evolution of the most intense peaks and of the amorphous bump with inclination angle, ϕ. The weight crystallinity X_c and the amorphous halo position $2\theta_a$ are indicated on each scan. The phenomena observed in Fig. 13 are present in this figure. From $\phi=0–90°$, the intensity of the peaks corresponding to the $(001)_m$, $(110)_o$, and $(200)_o$ planes and that of the amorphous bump are reinforced. Consequently, these planes and the amorphous diffraction entities get oriented along the tensile direction. It is important to remark that X_c and $2\theta_a$ increase as the inclination angle ϕ increases. In particular, we get $X_c=49\%$ and $2\theta_a=20.29°$ when $\phi=0°$, then $X_c=56\%$ and $2\theta_a=21.39°$ for $\phi=90°$.

A shift of the amorphous bump with applied strain has been already reported in the literature [14,48,49]. Following these authors, we ascribe this phenomenon to the modification of local molecular environment in the amorphous phase upon stretching. As a starting point, we define an 'apparent Bragg's distance' from the diffraction angle at the top of the amorphous bump: $d_a=\lambda/2\sin(\theta_a)$, where λ is the wavelength of the incident X-rays. For the undeformed samples, the above formula leads to an isotropic value: $d_a=0.428$ nm. This distance is related to the average distance between the close-neighboring molecular groups that diffract X-rays in the WAXS method. Obviously, the order of magnitude of d_a is too large to correspond to the distance between first or second CH_2 neighbors within chain skeleton. It is rather commensurable with the average interchain distance determined by non-polar van der Waals bonds.

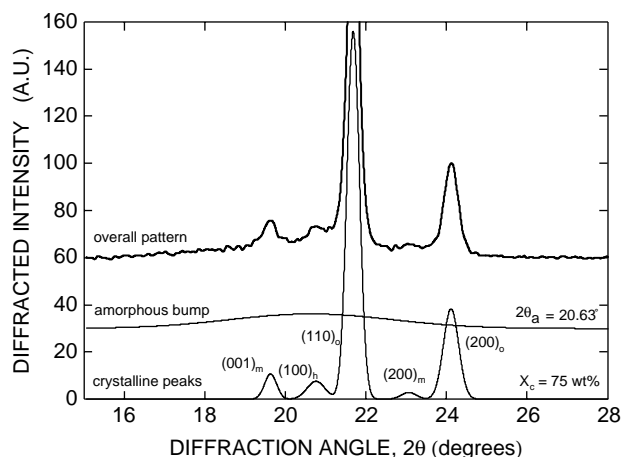Fig. 14. Deconvolution of the diffraction curve for a non-deformed sample (baseline was previously subtracted from the WAXS signal).
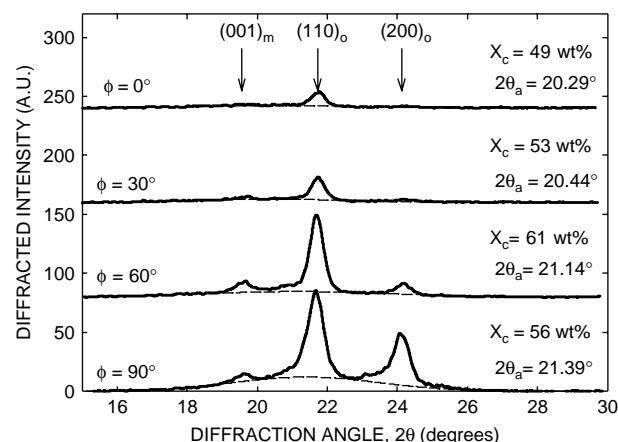

Fig. 15. Examples of 2θ scans of HDPE sample with a residual axial strain of 0.48 plotted at various azimuthal angles ϕ.

Diffraction analysis shows that amorphous interchain distance increases slightly with strain when measured along the axial orientation, while it decreases significantly along the transverse direction. For each level of residual strain, we define the average Bragg's distance of the amorphous phase by the equation:

$$\langle d_a \rangle = \frac{\int\limits_0^{\pi/2} d_a(\phi) I_a(\phi) \sin(\phi)\delta(\phi)}{\int\limits_0^{\pi/2} I_a(\phi)\sin(\phi)\delta(\phi)}.$$

In this relation, $I_a(\phi)$ represents the intensity of amorphous bump that varies with the azimuthal angle, ϕ. Through this computation, we obtain the evolution of $\langle d_a \rangle$ with ε_{33r} displayed in Fig. 16(a). Starting from the initial value, $\langle d_a \rangle = 0.428$ nm for the non-deformed state, the average Bragg's distance rapidly decreases with strain until residual strain reaches $\varepsilon_{33r}=0.2$, and more slowly for larger strains. The ultimate variation, for $\varepsilon_{33r}=1.3$, is equal to -2.6% compared with the initial microstructure. If we consider that $\langle d_a \rangle$ is a correct indicator of the average interchain distance, the above results provide an experimental evidence of a densification upon stretching in the disordered zones of the material.
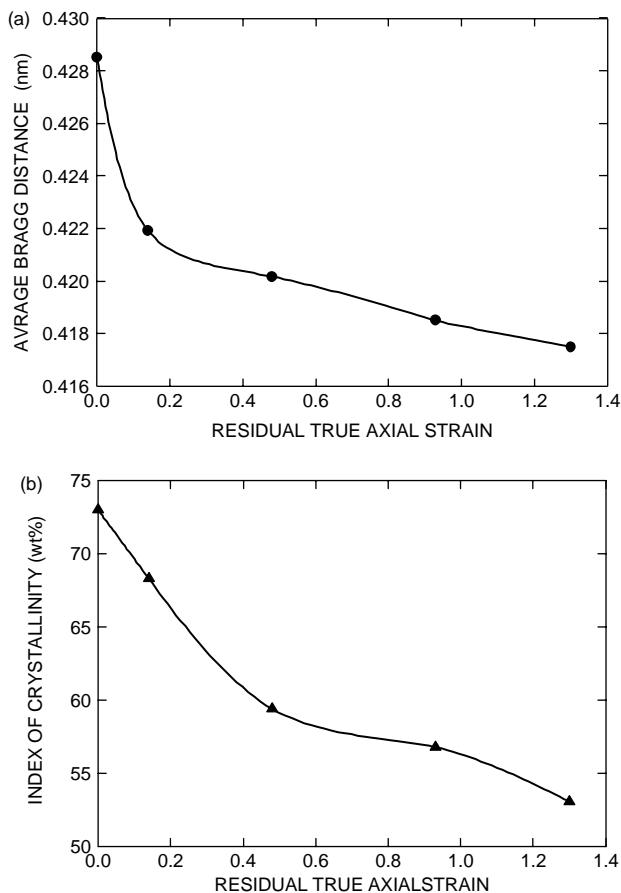

Fig. 16. Variation of (a) apparent Bragg's distance in the amorphous phase and (b) index of crystallinity of HDPE vs. residual strain after stretching, unloading and recovery.

Also the analysis of diffraction patterns gives access to information related to the crystalline phase. Using the simple procedure based on the relative surface of crystalline peaks and integrating this information over the complete range of azimuthal angle, we find (Fig. 16(b)) that the index of crystallinity decreases gradually from 73 to 53 wt% as residual strain increases from 0.0 to 1.3.

4. Discussion

4.1. Deformation mechanisms

4.1.1. Evolution of spherulitic morphology

Since, the amorphous phase of HDPE is rubbery at room temperature, the first deformation mechanism corresponds to the interlamellar extension and/or shearing, depending on the orientation of the crystallites with respect to the tensile axis [2,4–6,19,50]. Deformed amorphous chains are progressively oriented toward the principal tension axis of the local strain tensor. However, this process is limited by the severe confinement within the narrow interlamellar interstices and, furthermore, by finite extensibility of the highly entangled chains. Consequently, formation of micro-voids is likely to occur in the amorphous layers, especially in the equatorial zones of the spherulites or at inter-spherulitic boundaries [1,51,52], as shown in Fig. 10(a) and (b).

After a critical stress is attained, the crystalline lamellae are affected at their turn by dissipative deformation mechanisms. According to previous authors [4,6,13,19,53], plastic flow begins in diagonal zones of the spherulites by crystal plasticity, especially by slip parallel to the chains. This process, that readily accommodates most of the applied deformation, eventually leads to two secondary effects: (i) plastic tilt of crystallites toward the direction of tensile axis and, (ii) lamellar reorganization and fragmentation. This complex evolution is characterized by a decrease of crystallinity and gives rise to a fibrillar structure such as that observed in Fig. 10(c) and (d) at increasing strains. The alignment of the micro-fibrils with the tension direction is responsible for the hardening observed in the true stress vs. true strain curve of Fig. 4.

The inhomogeneous deformation of the spherulites described above is in line with the models introduced by many authors [1,13,36,54]. Within this scheme, the factors that promote the development of cavitation are: (i) weak mobility of the amorphous phase, (ii) low density of tie molecules and, (iii) inhomogeneous slip process of crystalline lamellae [55].

4.1.2. Volume strain processes

Four microscopic mechanisms compete in the control of volume strain: elastic expansion ($\Delta V > 0$), amorphous chain compaction ($\Delta V < 0$), crystalline order destruction ($\Delta V > 0$) and cavitation ($\Delta V > 0$).

Elastic expansion appears within the van der Waals solid under the effect of the hydrostatic stress. It is expressed either through the Poisson's ratio, ν or through the bulk modulus, $K = E/3(1-2\nu)$ [17,28,56,57].

The compaction of the amorphous phase is caused by the shrinkage of average distance between neighbouring chains while they are stretched and oriented between lamellae within the deformed spherulites. Our results confirm previous ones [20] who assessed volume variations in a low-density ethylene/butene copolymer with another video technique during tensile tests performed at 20 °C for a stretching rate of 0.5 mm/min. Like in our work, these authors noted a net volume compaction at the beginning of deformation. The authors invoked a strain-induced reorganization of the amorphous phase in sheared interlamellar zones. This process corresponds to a significant immobilization of amorphous chains that is otherwise revealed by dynamic mechanical analysis. This interpretation is supported by a previous author [14], who considered that chain alignment toward stretching direction in the amorphous phase tends to form a close-packed array with a pseudo-hexagonal symmetry. It is thus probable that the decrease of interchain distance in the amorphous phase (Fig. 16(a)) is the key process that controls the transient plastic compaction observed in HDPE upon stretching.

Crystalline order destruction begins when fragmentation is activated among the crystallites while the fibrillar structure is progressively formed. Through that process, crystallized chains are transferred into amorphous clusters. Previous studies [58,59] confirm the decrease of crystallinity in polyethylene during stretching until a draw ratio $\lambda = 5$ (that is for $\varepsilon_{33} \approx 1.6$). This process provokes a macroscopic dilatation since the density of the amorphous zones generated is lower than the density of crystallites.

However, cavitation is the main cause of dilatation at large strains. It starts in equatorial zones of spherulites, and continues by void multiplication, growth and coalescence as micro-fibrillation takes place. This dilatation phenomenon in semi-crystalline materials has been documented in details by many authors [17,19,22,29,60].

Since, strain rate increase induces decrease mobility of amorphous chains and increases yield stress of crystallites [12,19,55], cavitation in amorphous layers and fragmentation of crystalline lamellae are promoted earlier during faster tensile tests (Fig. 5).

It should be noticed that HDPE is not the only crystalline polymer that exhibits compaction and dilatation. Similar processes were identified in polypropylene [61,62]. In the latter material, compaction has been partly ascribed to orientation induced crystallization of the amorphous chains [63] and dilatation to high crazing susceptibility, especially in monoclinic α phase [52].

4.2. Volume strain decomposition

4.2.1. Modeling

Bucknall [28] has proposed in 1972 a decomposition of strain-induced dilatation that was adopted by many authors (e.g. [21,29,64]). In Bucknall's model, the overall volume variation δV is the sum of three components: (i) elasticity, δV^{el}, (ii) plasticity, δV^{pl} and, (iii) cavitation, δV^{ca}. In his scheme, Bucknall simplifies the problem by writing $\delta V^{pl} = 0$, under the assumption that plastic deformation results of isochoric shear mechanisms that supposedly keep constant the volume of the material.

In our work, we start again from the above decomposition but we rewrite it in the Hencky's strain formulation that gives: $\varepsilon_v = \varepsilon_v^{el} + \varepsilon_v^{pl} + \varepsilon_v^{ca}$. In this expression, we have $\varepsilon_v = \ln(V/V_0)$, $\varepsilon_v^{el} = \ln(V_{el}/V_0)$, $\varepsilon_v^{pl} = \ln(V_{pl}/V_{el})$, $\varepsilon_v^{ca} = \ln(V/V_{pl})$ where the volumes in question are: (i) V_0 the initial volume of the undeformed material, (ii) V_{el} the volume after elastic deformation, (iii) V_{pl} the volume of the solid matrix that undergone elastic and plastic deformation in the absence of cavitation, (iv) V the actual volume of the deformed material. The capacity to operate this additive decomposition, even at large deformation, is a virtue of the Hencky's strain concept.

In addition to the formal modification introduced above, our model differs from Bucknall's one by the fact that plastic strain is not supposed a priori to be an isochoric process. We take into account the volume variations induced in the polymer bulk by the activation of the macromolecular processes revealed by WAXS experiments: amorphous chain orientation (compaction) and crystalline order destruction (dilatation). Consequently, all three terms, ε_v^{el}, ε_v^{pl} and ε_v^{ca}, are potentially different from zero and are evaluated in details in the section below.

4.2.2. Evaluation of volume strain components

During stretching, the elastic volume strain is given by the following relation: $\varepsilon_v^{el} = (1 - 2\nu)\varepsilon_{33}^{el}$, where ν is the Poisson's ratio and ε_{33}^{el} the elastic strain. As such, it is evident that the intensity of the elastic volume strain is accessible through the initial slope of the volume vs. axial strain curves by: $1 - 2\nu = d\varepsilon_v^{el}/d\varepsilon_{33}^{el}$. By supposing that linear elasticity holds for polymers, the non-elastic volume strain contribution could be followed in real time during tensile test by the relation $\varepsilon_v^{pl} + \varepsilon_v^{ca} = \varepsilon_v - \varepsilon_v^{el} = \varepsilon_v - (1 - 2\nu)\varepsilon_{33}^{el} = \varepsilon_v - (1 - 2\nu)\sigma_{33}/E$. If in situ microstructural characterization techniques were applied during the test (e.g. simultaneous synchrotron X-ray diffraction and tomography), direct correlation of macroscopic strain and microscopic processes could be achieved while stretching. Here, we only dispose on post-mortem characterization techniques (WAXS and SEM), so that we perform such correlation on unloaded and recovered HDPE. Fortunately, thanks to the commutability of Hencky's strains, we can consider that the residual volume strain vs. residual axial strain envelope (Fig. 8) correctly represents the macroscopic contribution of $\varepsilon_{vr}^{pl} + \varepsilon_{vr}^{ca}$ in the unloaded and recovered state, and thus can be modeled in terms of the microscopic evolutions depicted in Fig. 16 (effects of residual plastic strain) and in Fig. 12 (cavitation).

Plastic volume strain in HDPE results on the opposite effects of crystalline destruction and amorphous chain compaction. The decrease of the index of crystallinity vs. applied strain is illustrated in Fig. 16(b). Here, we note X_c^0 and X_c^{pl} the weight percent crystallinity in the undeformed state and after a given amount of plastic strain, respectively. In the undeformed state, densities of crystalline and amorphous domains, ρ_c and ρ_a^0, are obtained from classical sources [26], which proves that ρ_a^0 is about 15% lower than ρ_c in HDPE. In

the plastically deformed material, the amorphous phase is relatively more abundant, but its density is higher than initially, due to the compaction of the amorphous chains revealed by X-ray diffraction. Quantitatively, we express the density increase by the relation: $\rho_a^{pl} = \rho_a^0[\langle d_a^0\rangle^3/\langle d_a^{pl}\rangle^3]$, where $\langle d_a^0\rangle$ and $\langle d_a^{pl}\rangle$ are the initial and current values of the average interchain distance directly obtained from the diffraction angle at the top of the amorphous bump (Fig. 16(a)). On the whole, the volume of a representative semi-crystalline element is obtained and readily leads to $\varepsilon_{vr}^{pl} = \ln[(X_c^{pl}/\rho_c) + (1-X_c^{pl})\langle d_a^{pl}\rangle^3/(\rho_a^0\langle d_a^0\rangle^3)] - \ln[X_c^0/\rho_c + (1-X_c^0)/\rho_a^0]$. In this expression, it is supposed that the density of the crystallites, ρ_c, is not affected by plastic deformation, since crystalline phase transformations on stretching are negligible in this case.

As for the effect of cavitation, we start from the evaluation of the surface void fraction, f_{vr}, measured in SEM micrographs (Fig. 12). It is important to notice that f_{vr} also characterizes the volume void fraction in the material. This simple topological property has been established by early authors [65,66] and it is correct providing: (i) strain gradients are small in the investigated RVE and, (ii) a large number of voids is considered. Both conditions are satisfied in our work since micrographs are obtained at the center of the RVE where cavitation is fairly homogeneous are present and because f_{vr} is calculated from 15 micrographs. Consequently, we have the operational relation: $\varepsilon_{vr}^{ca} = \ln(V/V_{pl}) = -\ln(1-f_{vr})$.

The quantitative data obtained from the investigation steps detailed above will now be displayed altogether to evaluate the correctness of our model. This is done through the plots in Fig. 17 that represent in the same graph the evolution with ε_{33r} of: (i) the residual plastic volume strain, ε_{vr}^{pl}, resulting from the balance of crystalline destruction and amorphous chain compaction and, (ii) the residual volume strain due to cavitation, ε_{vr}^{ca}. It is interesting to remark that plastic volume strain exhibits very small negative values (of the order of -0.01). This is because the effect of amorphous chain compaction is nearly compensated by the dilatation due to crystallinity loss during stretching. In the case of HDPE, this result corroborates a posteriori the assumption made by Bucknall [28] that volume effect in polymer plasticity is
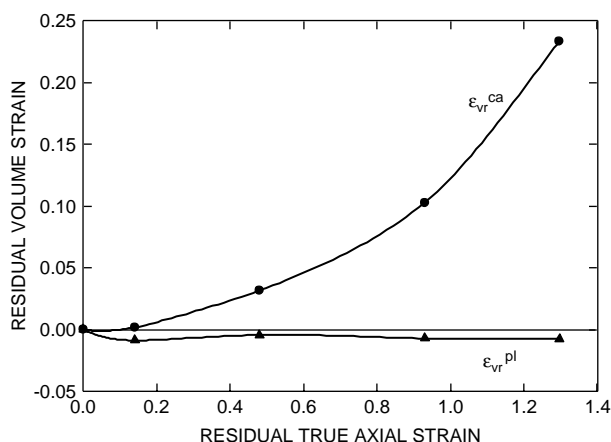
negligible. Here, we reach the same conclusion but we prove more precisely that it results from the balance of two non-negligible processes. Also, it would be useful to repeat the same protocol with other semi-crystalline polymers (e.g. isotactic polypropylene) to check if this property is general or specific for polyethylene. Furthermore, ε_{vr}^{ca} increases gradually with strain and reaches 0.23 for $\varepsilon_{33r}=1.3$.

Now, it is time to compare the volume strain information deduced from microstructural characterization (WAXS and SEM) and from the macroscopic analysis of VidéoTraction© results. The evolution with ε_{33r} of the non-elastic volume strain determined by the two methods is displayed in Fig. 18. It is interesting to note that both curves show the same shape: (i) small compaction in the early plastic regime and, (ii) important dilatation at large strains. This evolution is clearly in line with the deformation mechanisms analyzed in the preceding section. With both methods, it is found that the ultimate residual volume strain is about 0.2 for $\varepsilon_{33r}=1.3$, which proves that deformation damage should not be neglected when modeling the constitutive behavior of HDPE for structural applications.

The main discrepancy between the microstructural and macroscopic curves is in the plastic strain range between 0.0 and 0.8. It is noted in Fig. 18 that the compaction effect is less pronounced in the microscopic curve that in the VidéoTraction curve, the maximum difference being equal to about 0.04. At this state of the investigation, we are not capable to state unambiguously whether the discrepancy results on an over-estimation of volume strain at microscopic scale or by an underestimation of volume variation with VidéoTraction© device (or by both). Considering that residual cavitation is the most important component of microscopic volume strain, an overestimation of ε_{vr}^{ca} could be due to an imperfect adjustment of the contrast threshold and/or of the fibril density. On the other hand, an underestimation of macroscopic volume strain could be ascribed to the core algorithm of the VidéoTraction© system that does not fully takes into account the detailed deformation field during acute necking. A refined analysis of these two possible errors is now in progress.
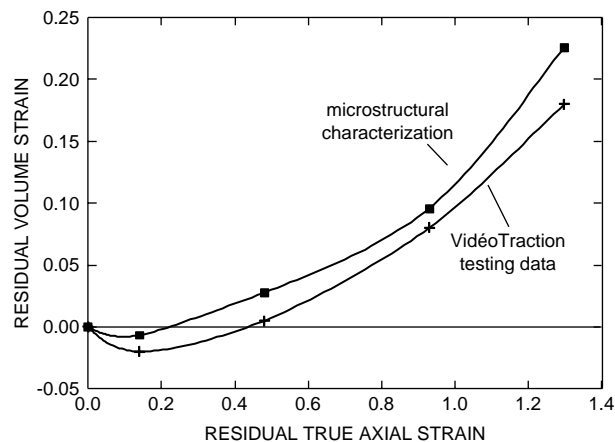

Fig. 17. Non-elastic volume strain components (plasticity and cavitation) in a series of stretched, unloaded and recovered HDPE samples.

Fig. 18. Final comparison of non-elastic volume strains determined in recovered samples after stretching by the VidéoTraction© method and by microstructural characterization (WAXS and SEM).

5. Conclusions

The volume strain of HDPE during tensile tests was investigated at the macroscopic scale by means of a 2D video extensometer (VidéoTraction[©]) and at the microscopic scale by X-ray diffraction and electron microscopy. Apart from the dilatation due to elastic deformation, which is small and can be easily isolated, the important volume strain upon stretching, larger than 30%, results from several macromolecular mechanisms that affect both the crystalline lamellae and the amorphous phase.

The most active process is the nucleation, growth and coalescence of voids within the semi-crystalline morphology. This non-cohesive mechanism begins by the localized formation of crazes inside or between the spherulites. Large interconnected cavitation develops in the polymer after the onset of crystalline fragmentation and, ultimately, while a highly fibrillated 'shish-kebab' structure is generated. When strain rate increases, amorphous chains have less mobility and severe cavitation appears in the deformation of crystalline lamellae. Consequently, earlier dilatation is noted at faster rates.

Particular attention was paid to the plastic deformation in the bulk. It was found (by analyzing WAXS patterns) that volume changes result from the competition between the dilatation effect due to gradual decrease of crystallinity upon stretching and the compaction effect caused by the orientation of macromolecular chains within the amorphous domains initially present.

The overall volume strain was decomposed into three components according to Bucknall's model: an elastic component, a plastic component and a cavitation component. However, in this work, the plastic volume strain was not neglected a priori but evaluated from the balance of crystalline order destruction and orientation-induced compaction in the amorphous phase. This evaluation was performed in the unloaded and recovered state, together with the assessment of void volume fraction. We confirmed Bucknall's assumption that plastic strain is isochoric ($\varepsilon_{vr}^{pl} \approx 0$), but this is only because the dilatation and compaction effects cancel each other. Also we found that the intensive deformation damage cause by crazing and cavitation is very important in HDPE since ε_{vr}^{ca} become larger than 0.2 at ultimate tensile strains.

Comparison of macroscopic volume strain (assessed by the VidéoTraction[©] system) and microscopic volume strain (evaluated from WAXS and SEM) shows the same general tendency, marked by small compaction in the early plastic stage and important dilatation at large strains. However, the volume strain deduced from microstructural analysis exhibits an excess discrepancy by comparison to mechanical testing data. The absolute difference is small, but its recurrent observation invites us to identify its source, either through a more accurate evaluation of void fraction from SEM micrographs, or by a better evaluation of strain field in the necked region of the tensile specimens.

It would be interesting to study the phenomena analyzed in this work for other deformation paths (compression, simple shear, biaxial stretching) and other loading programs (particularly in creep at constant true stress). Also the application of the experimental protocol to other materials (different polyethylene grades and other semi-crystalline polymers) would be worthwhile in order to check the generality of the processes investigated here. At last, it would be useful for mechanical designers to build a quantitative database with the constitutive equations of polymers that exhibit volume strain within formalism adapted for their implementation in finite element prediction of structural parts. All these research projects are presently in progress in this laboratory and in other institutes.

Acknowledgements

References

[1] Hay IL, Keller A. Koll Zeit u Zeit Polym 1965;204:43–74.
[2] Peterlin A. J Mater Sci 1971;6:490–508.
[3] Peterlin A, Meinel G. Makromol Chem 1971;142:227–40.
[4] Schultz J. Polymer materials science. Englewood Cliffs, NJ: Prentice-Hill; 1974 p. 466–511.
[5] Wade Adams W, Yang D, Thomas EL. J Mater Sci 1986;21:2239–53.
[6] G'Sell C, Dahoun A. Mater Sci Eng 1994;A175:183–99.
[7] Butler MF, Donald AM, Ryan AJ. Polymer 1997;39:39–52.
[8] G'Sell C, Jonas JJ. J Mater Sci 1979;14:583–91.
[9] G'Sell C, Hiver JM, Dahoun A, Souahi A. J Mater Sci 1992;27:5031–9.
[10] Hiss R, Hobeika S, Lynn C, Strobl G. Macromolecules 1999;32: 4390–403.
[11] Hillmansen S, Hobeika S, Haward RN, Leevers PS. Polym Eng Sci 2000; 40:481–9.
[12] Hobeika S, Men Y, Strobl G. Macromolecules 2000;33:1827–33.
[13] Lin L, Argon AS. J Mater Sci 1994;29:294–323.
[14] Bartczak Z, Galeski A, Argon AS, Cohen RE. Polymer 1996;37:2113–23.
[15] Powers JM, Caddell RM. Polym Eng Sci 1972;12:432–6.
[16] Mallon PJ, McCammond D, Benham PP. Polym Eng Sci 1972;12:420–4.
[17] Naqui SI, Robinson IM. J Mater Sci 1993;28:1421–9.
[18] Meddad A, Fisa B. J Appl Polym Sci 1997;64:653–65.
[19] Castagnet S, Gacougnolle JL, Dang P. Mater Sci Eng 2000;A276:152–9.
[20] Gaucher-Miri V, Depecker C, Seguela R. J Polym Sci 1997;35:2151–9.
[21] Quatravaux T, Elkoun S, G'Sell C, Cangemi L, Meimon Y. J Polym Sci 2002;40:2516–22.
[22] Gloaguen JM, Lefebvre JM. Polymer 2001;42:5841–7.
[23] G'Sell C, Hiver JM., French Patent # 010542100, Bull Off INPI, 23 April: 2001.
[24] G'Sell C, Hiver JM, Dahoun A. Int J Solids Struct 2002;39:3857–72.
[25] Amornsakchai T, Olley RH, Basset DC, Al-Hussein MOM, Unwin AP, Ward IM. Polymer 2000;41:8291–8.
[26] Wunderlich B. Macromolecular physics. Crystal structure, morphology, defects, vol. 1. New York, NY: Academic Press; 1973.
[27] Chivers RA, Barham PJ, Martinez-Salazar J. J Polym Sci 1982;20: 1717–32.
[28] Bucknall CB, Clayton D. Rubber-toughening of plastics, Part 1: Creep mechanisms in HIPS. J Mater Sci 1972;7:202–10.
[29] Pukanszky B, Van Es M, Maurer FHJ, Voros G. J Mater Sci 1994;29: 2550–8.

[30] Olley RH, Hodge AM, Basset DC. J Polym Sci 1979;17:627–43.

[31] Olley RH, Basset DC. Polymer 1982;23:1707–10.

[32] Kakudo M, Kasai N. X-ray diffraction by polymers. Tokyo, Japan: Kodansha Ltd; 1972 [Elsevier, Amsterdam and New York].

[33] Galeski A, Argon AS, Cohen RE. Macromolecules 1991;24:3945–52.

[34] Glenz W, Peterlin A. In: Peterlin A, editor. Plastic deformation of polymers. New York, NY: Marcel Dekker; 1971. p. 13–29.

[35] Kausch HH. Polymer fracture. Berlin, Heidelberg: Springer-Verlag; 1978 p. 15–39.

[36] Breedon JE, Jackson JF, Marcinkowski MJ, Taylor JME. J Mater Sci 1973;8:1071–82.

[37] Abo el Maaty MI, Basset DC. Polymer 2001;42:4957–63.

[38] Patel D, Basset DC. Polymer 2002;43:3795–802.

[39] Lotz B, Cheng SZD. Polymer 2005;46:577–610.

[40] Luo WB, Yang TQ, Wang XY. Polymer 2004;45:3519–25.

[41] Dasari A, Misra RDK. Mater Sci Eng 2004;A367:248–60.

[42] Schirrer R. In: G'Sell C, Haudin JM, editors. Introduction à la mécanique des polymèrs. Nancy, France: INPL; 1995. p. 395–411.

[43] Friedrich K. Adv Polym Sci 1983;52/53:225–74.

[44] Nakayama K, Kanetsuna H. J Mater Sci 1975;10:1105–18.

[45] Seto T, Hara T, Tanaka K. Jap Jour Appl Phys 1968;7:31–42.

[46] Vickers ME, Fischer H. Polymer 1995;36:2667–70.

[47] Tsubakihara S, Nakamura A, Yasuniwa M. Polym J 1991;23:1317–24.

[48] Salazar MJ, Ortega JCG, Calleja FJB. Anales de Fisica 1977;73:244–7.

[49] Murphy NS, Minor H, Bednarczyk C, Krimm S. Macromolecules 1993; 26:1712–21.

[50] Petermann J, Schultz JM. J Mater Sci 1978;13:50–4.

[51] Friedrich K. Progr Coll Polym Sci 1979;66:299–309.

[52] Aboulfaraj M, G'Sell C, Ulrich B, Dahoun A. Polymer 1995;36: 731–42.

[53] Haudin JM. In: Plastic deformation in amorphous and semi-crystalline materials. Les Ulis, France: Les Editions de Physique; 1982. p. 291–311.

[54] Predecki P, Thornton AW. J Appl Phys 1970;41:4342–6.

[55] Gaucher-Miri V, Séguéla R. Macromolecules 1997;30:1158–67.

[56] Whitney W, Andrews RD. J Polym Sci 1967;C16:2981–90.

[57] Pampillo CA, Davis LA. J Appl Phys 1971;42:4674–9.

[58] Glenz W, Morosoff N, Peterlin A. Polym Lett 1971;9:211–7.

[59] Meinel G, Peterlin A. J Polym Sci 1971;A2-9:67–83.

[60] Cessna LC. Polym Eng Sci 1974;14:696–701.

[61] Zok F, Shinozaki DM. J Mater Sci 1987;22:3996–4001.

[62] Tang HI, Hiltner A, Baer E. Polym Eng Sci 1987;27:876–86.

[63] Benham PP, McCammond D. Plast Polym 1971;130–6.

[64] Heikens D, Sjoerdsma SD, Coumans WJ. J Mater Sci 1981;16:429–32.

[65] Delesse A. Annales des Mines (Paris) 1848;13:379–88.

[66] Hilliard J.E. DeHoff R.T. Rhines F.N. editors. Quantitative microscopy, part 3: measurement of volume in volume; 1968, 45–76.